




Air-cushioning below an impacting wave-structured disk: Free-surface deformation and slamming load

Yee Li (Ellis) Fan ^{*}, Utkarsh Jain , and Devaraj van der Meer [†]

Physics of Fluids Group and Max Planck Center Twente for Complex Fluid Dynamics, MESA+ Institute and J. M. Burgers Centre for Fluid Dynamics, University of Twente, P.O. Box 217, 7500AE Enschede, The Netherlands



(Received 15 June 2023; accepted 6 December 2023; published 10 January 2024)

Prior to the impact of a horizontal disk onto a liquid surface, the air underneath flows radially outward across the liquid surface to escape from below the edge of the disk. Such airflow causes the surface to be elevated near the disk edge, creating a free-surface condition that influences the details of the subsequent impact dynamics. In this work, the nature of the surface elevation under an impacting disk is investigated by modulating the forcing of the free surface: The airflow below the disk is altered by imposing a radially symmetric wave structure of varying wavelength on the impacting disk surface. Subsequently, the liquid surface deformation before impact is measured experimentally using a total internal reflection technique. The experiments provide convincing evidence that supports the argument that the surface elevation is an instability of the Kelvin-Helmholtz type. In addition, the impact force exerted on the wave-structured disks is measured using a load cell. Due to the macroscopic wave structure on the disk, the maximum impact force is significantly reduced, and the results indicate that both the free-surface deformation before impact and the way in which the impacting surface is subsequently wetted influence the maximum impact force.

DOI: [10.1103/PhysRevFluids.9.010501](https://doi.org/10.1103/PhysRevFluids.9.010501)

I. INTRODUCTION

Solid-liquid impact problems have been widely investigated due to their relevance in a multitude of applications, ranging from large-scale events in the marine or ocean industries such as the landing of seaplanes [1,2], wave impact on harbours [3], and sloshing in fuel transportation tanks [4] to smaller-scale occasions like jumping of waters striders [5]. One of the classical solid-liquid impact problems is the impact of a horizontal disk onto a liquid bath and previous studies all highlighted the significance of the ambient air on the impact dynamics [6–9].

The presence of ambient air during solid-liquid impact was found to have a notable influence both before and during the impact process. It was reported that, prior to the impact of a flat disk, the airflow between the disk and the liquid surface deforms the free surface in a manner that the central region is depressed due to the stagnation point at the center while the free surface near the disk edge is elevated, forming a wave shape due to the high escaping air velocity at the disk edge. Although there are several mechanisms for the generation of surface waves in a concurrent flow of air and water, for example through the transmission of energy due to the pressure variation at the interface [10] or a resonance mechanism [11], such free-surface elevation under an impacting disk was argued to be regarded as a type of Kelvin-Helmholtz instability [7,12]. The free-surface

*y.l.fan@utwente.nl

†d.vandermeer@utwente.nl

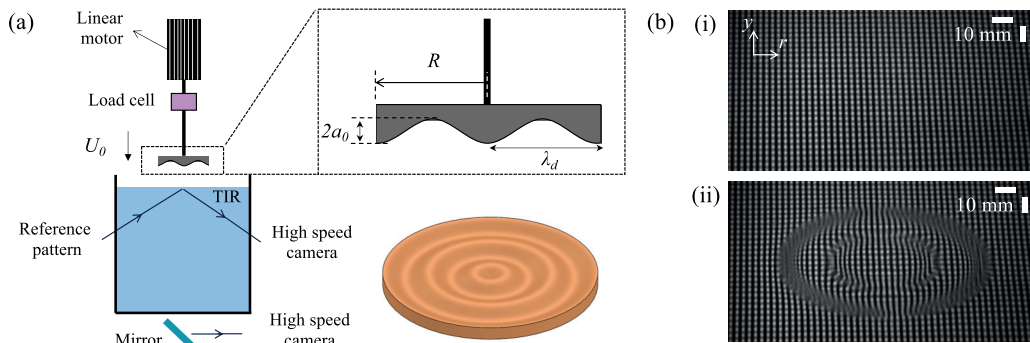


FIG. 1. (a) Schematic of the experimental set-up and the geometry of a 3D printed disk with radially symmetric sinusoidal wave structure. All the wave-structured disks used in the experiment have the same radius R and amplitude a_0 but different wavelength λ_d . The disk edge always coincides with a crest of the wave structures. (b) (i) Reflected reference grid pattern imaged by the high-speed camera using the total internal reflection (TIR) setup when the water surface is stationary. (ii) Distorted image of the reference pattern when the water surface is perturbed due to the approaching disk.

elevation incurs at the free surface when the air velocity exceeds a critical velocity and a dominant unstable wavelength λ_{marg} , which is determined by the competition between gravity and surface tension emerges at the onset of instability in accordance with the nature of Kelvin-Helmholtz's instability [12,13]. For water and air, in ambient conditions, the dominant unstable wavelength λ_{marg} is found to be approximately 1.7 cm [11,12], and occurs where the air velocity is expected to be the largest, namely below the edge of the disk.

Subsequently, the free-surface deformation results in the entrapment of a thin layer of air in between the free surface and the disk as it plunges into the liquid, which was confirmed in previous experimental studies [7,8,12]. In general, such a trapped air layer interferes with the direct interaction of solid and liquid and therefore plays a crucial role in determining the load on the solid body [2,4,14]. A trapped air layer is well-known to provide an air-cushioning effect that may be effective in reducing the maximum hydrodynamic loading [15,16] and may also affect the load distribution on the solid body during water impact [17], but it can also increase the duration at which the loading is exerted on the impacting surface [9,16,18].

In this study, we will manipulate the way that the impacting object is forcing the free surface by structuring the flat surface with a well-defined wavelength: A radially symmetric sinusoidal wave structure of different wavelengths is imprinted on the impacting surface of the disk to modulate the escaping airflow underneath the disk and the growth of the instability at the free surface is studied experimentally. On top of that, the effect of the surface profile of the impacting disk on the impact dynamics and the hydrodynamic loading exerted on the disk is also investigated to identify the factors that could affect the peak impact force and the impact duration during the water impact of a wave-structured disk.

II. EXPERIMENTAL SETUP

As depicted in Fig. 1, the experimental setup consists of a 50 cm \times 50 cm \times 80 cm transparent glass tank, filled with demineralized water at a water level of 30 cm. Disks with radially symmetric sinusoidal wave structures of different wavelength λ_d are printed with a 3D printer (Formlabs, Form 2) using Model V3 or white resin. The radius R and the amplitude of the wave structure a_0 are 40 and 1.25 mm, respectively, for all the disks. A $R = 40$ mm flat aluminium disk is also used to compare with the wave-structured disks.

The impact motion is controlled using a linear motor (NITEK, GDP350XS750G2). The disk is connected to the linear motor by means of a rod and is impacted vertically onto the water bath with its impacting surface parallel to the free water surface. The linear motor accelerates within a short time interval to reach the constant, programed impact velocity U_0 which is fixed at 1.0 m/s in this experiment. The disk is allowed to travel a minimum distance of 0.3 m before making contact with the free water surface to ensure the impact velocity is constant when the disk is close to the free surface and during the impact.

The deflection of the free water surface prior to impact is visualized using the total internal reflection (TIR)-based measurement technique [19]. The free water surface acts as a mirror to reflect a reference grid pattern that is illuminated by a panel light source underneath. The reference pattern is placed horizontally at a position where the angle of incidence at the water-air interface is approximately 56° . An undisturbed reference grid pattern is reflected by the free water surface and imaged by a high-speed camera at a frame rate of 30 000 f.p.s (Photron, Nova S16 or S12), as shown in Fig. 1(b(i)). As the disk approaches the free water surface, the water surface is perturbed which results in the distortion of the image of the reference pattern that is being reflected toward the camera [Fig. 1(b(ii))]. The displacement of the reference grid is then quantified using PIV and correlated to the water surface deformation to obtain a three-dimensional reconstruction of the water surface. The details of this procedure are described in Ref. [19].

The subsequent process of the disk's impact into the water bath was captured separately from the bottom using a high-speed camera at 50 000 f.p.s using a mirror and LED light sources illuminating the bottom of the disk. The focal plane is located at the free surface. An analog strain gauge load cell (FUTEK, LSM300) with a maximum loading capacity of ≈ 227 kg and natural frequency of 2499 Hz is also mounted on the rod to measure the overall force on the disk that is generated as the disk plunges into the water bath. The measurements were done at an acquisition rate of 10 kHz using an analog amplifier with current output (FUTEK, IAA200).

III. MODULATION OF THE ESCAPING AIRFLOW UNDER AN IMPACTING DISK

Referring to Fig. 2(a), by assuming a slender gap d between the undeformed free surface and the bottom of the impacting disk ($d \ll R$), the air is squeezed out mainly in the radial direction; thus $V_z \ll V_r$. In the air gap under a flat disk, the height-averaged radial velocity profile of air $V_{r,\text{flat}}$ can be obtained using the depth-integrated continuity equation [12]:

$$V_{r,\text{flat}}(\tau) = \frac{U_0 r}{2d(t)} = \frac{r}{2\tau}, \quad (1)$$

where r is the radial coordinate (with $r = 0$ the location under the disk's center) and $\tau = t_{\text{impact}} - t$ is the time before impact (with $\tau = 0$ the moment of impact, i.e. $d = U_0\tau$, when the deformation of the interface is neglected). When generalizing the expression for a wave-structured disk, the moment of impact is defined as the time when the crests of the wave structure would touch the undeformed water surface. For a disk with a radially symmetric sinusoidal wave structure, the gap d becomes a function of both the time before impact τ and the radial coordinate r :

$$d(r, \tau) = U_0\tau - a_0 \cos \left[\frac{2\pi}{\lambda_d}(R - r) \right] + a_0. \quad (2)$$

Note that a minimum of $d(r, \tau)$ is always located at the disk edge ($r = R$) for which $d(R, t) = U_0\tau$. Similarly, from the continuity equation, the resulting equation for the height-averaged radial velocity of the air under a wave-structured disk can be written as

$$V_r(r, \tau) = \frac{U_0\tau}{2d(r, t)} = \frac{r}{2\tau + 2\tau_0 - 2\tau_0 \cos[k(R - r)]}, \quad (3)$$

where $k = 2\pi/\lambda_d$ and $\tau_0 = a_0/U_0$. It is clear that the wave structures modulate the airflow by introducing the term $\cos[k(R - r)]$ in the denominator that, for sufficiently small τ , induces alternating

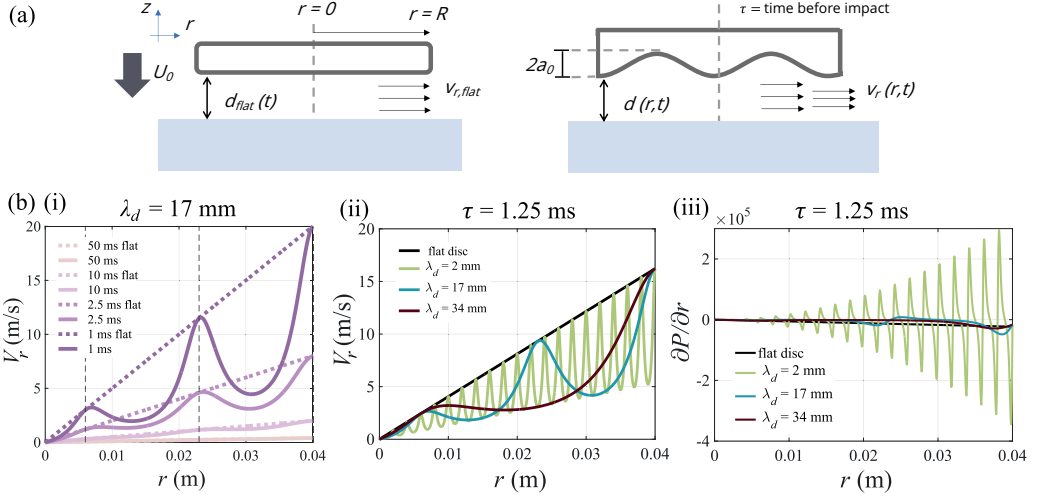


FIG. 2. (a) Schematic to derive the theoretical estimate for the air velocity profile under a flat disk and a disk with radially symmetric sinusoidal wave structure. (b) (i) Temporal evolution of the theoretical velocity profile of air under a $\lambda_d = 17$ mm disk (solid lines) and a $R = 40$ mm horizontal flat disk (dotted lines). While the air velocity increases linearly across the radial coordinates for a flat disk, velocity maxima and minima are induced under a wave-structured disk as the time before impact τ decreases. The locations of the velocity maxima and minima are closely located under the crests of the wave structure (indicated by the vertical dashed lines) on the disk. (ii) Comparison of the theoretical velocity profile of air under a $R = 40$ mm flat disk and $\lambda_d = 2, 17, 34$ mm disks at $\tau = 1.25$ ms. (iii) Pressure gradient of air for the selected disks at $\tau = 1.25$ ms.

velocity maxima and minima. The local velocity maxima and minima are expected to be induced close to the crests and troughs of the wave structures, respectively.

Since $d \ll R$, by taking the averaged radial velocity $V_{r,\text{avg}}$ and air gap width d_{avg} over the radial distance, the Reynolds number of the modulated airflow, $\text{Re} = \rho_a V_{r,\text{avg}} d_{\text{avg}} / \mu_a$, where ρ_a and μ_a are the density and the dynamic viscosity of air, respectively, is much greater than 1 throughout the descending motion for all the disks in the experiment. Thus, the airflow under the impacting disk is in an inertial-thin gap regime, where viscous effects are relatively insignificant.

Normalizing Eq. (3) with Eq. (1) gives

$$\tilde{V}_r(r, \tau) = \frac{1}{1 + \frac{\tau_0}{\tau} - \frac{\tau_0}{\tau} \cos[k(R - r)]}. \quad (4)$$

The normalized velocity maxima $\tilde{V}_{r,\text{max}}$ are bounded to 1 while the normalized velocity minima are given by $\tilde{V}_{r,\text{min}} = \tau / (\tau + 2\tau_0)$. Initially, $\tilde{V}_{r,\text{min}} \approx \tilde{V}_{r,\text{max}} \approx 1$ when τ is relatively large. Taking reference to a $\lambda_d = 17$ mm disk, at the beginning stage where τ is relatively large (50 and 10 ms), the radial velocity V_r shows negligible differences as compared to a flat disk, as shown in Fig. 2(b(i)). The difference between \tilde{V}_{max} and \tilde{V}_{min} becomes pronounced (larger than a factor of 2) when $\tau \lesssim 2\tau_0$. Therefore, as the disk descends ($\tau = 2.5$ ms and 1 ms), clear local velocity maxima and minima are induced due to the modulation of airflow by the wave structures. The location of the local velocity maxima is closely located under the crests of the wave structure which are indicated by the vertical dashed lines.

By changing the wavelength of the wave structure imprinted on the disks, different modulations of the airflow underneath the disks can be achieved as seen in Fig. 2(b(ii)). The quantity $\kappa_d = R/\lambda_d$ determines the number of local velocity maxima. Short wavelengths (e.g., $\lambda_d = 2$ mm) give more velocity maxima and minima with steep velocity gradient while a longer λ_d , e.g., $\lambda_d = 17$ mm, has fewer velocity maxima and minima but the width of the velocity peaks is wider and thus

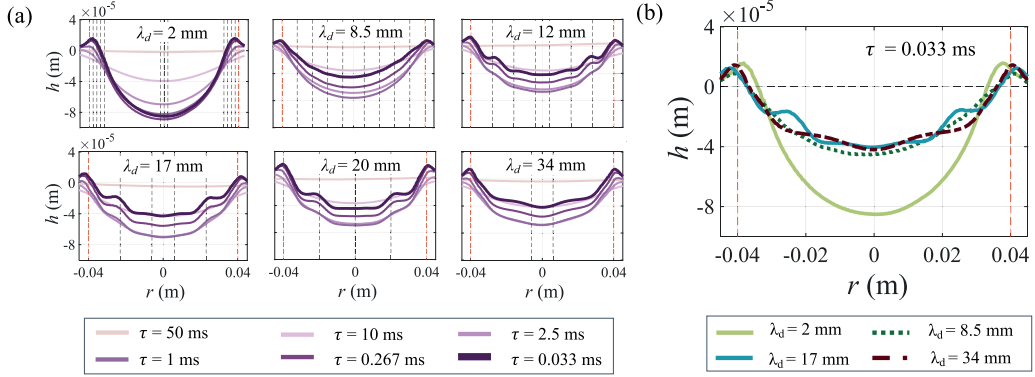


FIG. 3. (a) Six snapshots from the temporal deformation of the water surface before impact taken at the y -center plane, for disks with imprinted wavelength λ_d of 2, 8.5, 12, 17, 20, and 34 mm. The results for the other disks are shown in the Supplemental Material [20]. The vertical dashed lines indicate the location of crests on the impacting disk. In the figure for $\lambda_d = 2$ mm disk, most of the dashed lines were omitted for clarity. The red vertical dashed lines denote the disk edge as well as the crest located at that point. Note that by virtue of the impact speed used in these experiments ($U_0 = 1.0$ m/s), times before impact τ denoted in ms can be easily converted to the distance of the crests of the disk to the undisturbed interface in mm. (b) Cross-sectional profile of the free surface taken at the y -center plane, right before the disk makes first contact with the water surface ($\tau = 0.033$ ms) for four selected disks ($\lambda_d = 2, 8.5, 17,$ and 34 mm).

the velocity gradient is less steep. The difference in the air velocity profile gives rise to different forcing pressure and shear stress distribution over the water surface. These generate small forced oscillations, and depending on the response of the water surface to the wave number of the forcing, the continued presence of these components may influence the growth of the instability. From the inviscid momentum equation in the radial direction,

$$\rho_a \frac{\partial V_r}{\partial t} + \frac{\partial}{\partial r} \left(\rho_a \frac{V_r^2}{2} + P_a \right) = 0, \quad (5)$$

the pressure gradient can be estimated as

$$\frac{\partial P_a}{\partial r} = -\rho_a \left(\frac{\partial V_r}{\partial t} + V_r \frac{\partial V_r}{\partial r} \right). \quad (6)$$

The pressure gradient is plotted as a function of the radial coordinate at $\tau = 1$ ms for selected disks in Fig. 2(b(iii)). Adverse pressure gradient ($\frac{\partial P}{\partial r} > 0$) are formed at the leeward side of the crests, especially for disks with a short or intermediate wavelength. Meanwhile, for long wavelengths, e.g., $\lambda_d = 34$ mm, the pressure gradient is always favourable ($\frac{\partial P}{\partial r} < 0$) for the airflow to exit and higher than the flat disk around the disk edge region, suggesting a more accelerated flow at the exit gap for a wave-structured disk as compared to a flat disk. Forcing on the water surface is produced due to the pressure gradient in the airflow that is directed from the high-pressure to the low-pressure region. Clearly, the expressions derived in this section are approximate since they are all based on height-averaged inviscid theory. Nevertheless, in view of the rapid acceleration of the airflow, they at least qualitatively provide a good impression of the velocity and pressure distributions below the disk during the impact. In the next section, we will use this knowledge in interpreting the surface deformation data obtained in the experiment.

IV. DEFORMATION OF THE FREE SURFACE BEFORE IMPACT

Figure 3(a) shows six snapshots from the temporal evolution of the free-surface profiles taken at the y -center plane $h(r, \tau)$ plotted as a function of the radial coordinate r before impact for the wave-structured disks with various wavelengths λ_d , namely $\lambda_d = 2, 8.5, 12, 17, 20,$ and 34 mm. The surface deformation during the initial stages resembles the free-surface profile under a flat horizontal disk [12]: The initially quiescent liquid-air interface at $\tau = 50$ ms is pushed down gradually by the airflow with time and forms an air cavity at the water interface. In addition, in the later stage before impact ($\tau \leq 1$ ms), the elevation of the free surface close to the disk edge is observed. It is this elevation at the disk edge that had been interpreted as a type of Kelvin-Helmholtz instability in Ref. [12]. Both depression and elevation of the free surface are seen for all the disks tested in the experiment as presented in Fig. 3(a) and the Supplemental Material [20].

Nevertheless, the water cavity dynamic for the wave-structured disks is distinct from that of a flat disk. The disk with the shortest wavelength ($\lambda_d = 2$ mm) produces cavities that are similar to that of a flat disk, where the cavity depth tends towards a maximum [12]. The final depth of the water cavity at $\tau = 0.033$ ms for $\lambda_d = 2$ mm disk ($h_f = -8 \times 10^{-5}$ m) is comparable to that of a flat disk ($h_f = -12 \times 10^{-5}$ m, Supplemental Material [20]). However, for all wave-structured disks with a larger wavelength ($\lambda_d > 2$ mm), the water cavity reaches a maximum depth at approximately the same time before impact (around $\tau = 1$ ms) and subsequently retracts upward. Retraction becomes more pronounced with increasing λ_d . Comparing a $\lambda_d = 8.5$ mm and $\lambda_d = 2$ mm disk, the final depth for a $\lambda_d = 8.5$ mm disk is approximately halved. The maximum and final depth of the water cavity becomes similar when $\lambda_d \geq 8.5$ mm, as seen in the plots in Fig. 3. The depth of the cavity is mainly an inertial effect [12]. By integrating Eq. (6) to get an estimation of the pressure distribution on the water surface (see the Supplemental Material [20]), the magnitude of the pressure under the disk center for a flat disk is always substantially larger than that of a wave-structured disk. The increment of pressure with time for a flat disk is also significantly steeper as compared to a wave-structured disk. This could be one of the reasons for the smaller final depth and the overall retraction of the cavity for a wave-structured disk. On top of that, the growth of instabilities may also interfere with the cavity dynamics as these may influence the air velocity profile, especially when the air gap is small, causing the cavity dynamics to slightly change.

Apart from the overall retraction of the cavity, another major difference between a flat disk and a wave-structured disk with intermediate and long wavelength ($\lambda_d > 8.5$ mm) is that, in addition to the surface elevation near the disk edge, new sites of surface elevation appeared within the water cavity. This is clearly seen in Fig. 3(b), where the free-surface profile just before impact (at $\tau = 0.033$ ms) is plotted for four selected disks. These new sites of surface elevation within the water cavity (to be known as secondary instabilities hereafter), when aroused significantly for disks with intermediate wavelength, are located closely under the crests of the wave structure of the disk [indicated by the vertical dashed lines in Fig. 3(a)], agreeing with what is suggested by the theoretically predicted airflow profile that the induced local velocity maxima are located near the crests. In contrast, for long wavelengths on the disks, e.g., $\lambda_d = 34$ mm, the location of secondary instabilities shifts away from the crests as shown in Fig. 3(a), where the black vertical dashed lines do not align with the secondary instabilities. Previously, secondary instabilities were also observed in Ref. [8] during shallow water impact of a $D = 160$ mm circular disk with a slightly concave impacting surface, where a second circular wave structure was formed at a radial distance of about 2 cm inward from the disk edge.

Meanwhile, disks with short imprinted wavelength ($\lambda_d < 8.5$ mm) have the same global cavity shape as a flat disk in the sense that secondary instabilities are absent. For these disks with short imprinted wavelengths, the modulated airflow is attempting to force the water surface to manifest short wavelengths, or capillary waves at the interface. There are several possible reasons for the absence of the secondary instabilities. First, instabilities with a short wavelength that are triggered at points that are very close to one another are hard to differentiate from a flat surface, especially when the amplitude is small. Besides, in the framework of Kelvin-Helmholtz instability, surface

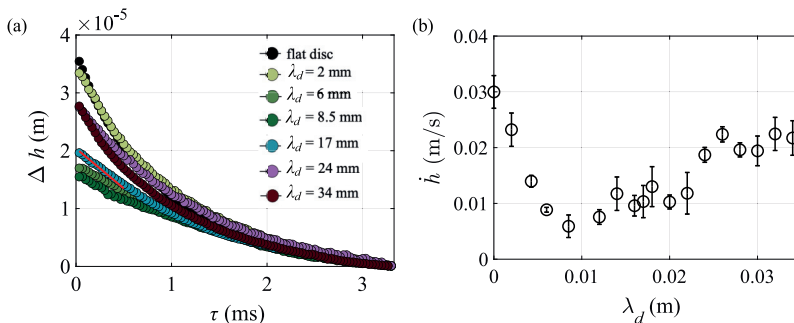


FIG. 4. (a) Time evolution of the growth of the primary instability Δh under the disk edge (P1) for selected wave-structured disks. The starting time, for which $\Delta h = 0$, was taken as $\tau = 3.33$ ms as P1 started to increase monotonically around this time for all the wave-structured disks used in the experiment. (b) Plot of the time derivative \dot{h} of Δh [red solid slope line in panel (i)] taken from $\tau = 0.033$ ms to 0.5 ms, for all the disks. $\lambda_d = 0$ m corresponds to a $R = 40$ mm flat disk. Error bars represent the standard deviation of \dot{h} over three repetitions of the experiment for each disk.

tension stabilises the capillary waves. Therefore, the initiation and growth of short wavelengths at the air-water interface will have to first overcome the surface tension of the water. The restoring force of surface tension is proportional to the curvature of the surface, while the curvature of the surface is inversely proportional to the wavelength. Hence, a shorter wavelength wave will experience a higher surface tension force that prohibits its initiation and growth, which explains why the shape and cavity dynamics of the shortest wavelength disk $\lambda_d = 2$ mm resemble a flat disk. In addition, as mentioned in Sec. III, the forcing on the water surface is produced due to the local velocity maxima and minima which give the radial pressure gradient in the airflow. Note that the adverse pressure gradient, which does not favour the exit airflow, is especially large for disks with short imprinted wavelengths [see Fig. 2b(ii)]. These adverse pressure gradients could induce boundary layer separation of the airflow at the leeward side of the crests, making the airflow over a disk with a short wavelength similar to a flat disk. However, since the Reynolds number of the airflow is relatively high, we expect this flow separation effect to be a less prominent factor.

As the forcing wavelength on disks λ_d increases, waves try to develop on the water surface at a distance λ_d , competing with the restoring surface tension force. However, it appears to be that the forcing from the wave-structured disk is insufficient to supply the required energy for the growth of these relatively short wavelengths, and it only causes the overall retraction of the water cavity and in some cases a minute, almost indiscernible perturbation within the cavity at the very late stage, as seen in Fig. 3(a) for $\lambda_d = 8.5$ mm. With the increase of λ_d up until 8.5 mm, the overall retraction of the water cavity is accompanied by the attenuation of the amplitude of the primary instability, which is the surface elevation under the disk edge, as evidenced in Fig. 3(a) ($\lambda_d = 2$ and 8.5 mm).

A. Amplitude of the primary instability

To better understand the development of the primary instabilities, the temporal growth of the surface elevation Δh under the edge of the disks is tracked, and the results for 6 selected disks and a flat disk are plotted in Fig. 4(a). The amplitude of the primary instabilities for all the disks was observed to increase monotonically from around $\tau = 3.33$ ms, which is therefore taken as the zero reference time. The growth of the instability Δh plotted here is, therefore, the averaged instantaneous height at a fixed position (where the amplitude of the primary instability is maximum at the final frame from the cross-sectional profile) under the disk edges $h(\tau)$ minus $h(\tau_0)$ at $\tau_0 = 3.33$ ms. The fact that the primary instability starts to develop at approximately the same time reflects that the time at which the critical velocity is reached under the disk edge is similar for all the disks,

as expected from the expressions in Eq. (3). Initially, the amplitude of the primary instabilities for all the disks increases slowly at a similar rate, but towards the final 1 ms before impact, they show a notable difference. While the amplitude for a $\lambda_d = 2$ mm disk is similar to a flat disk, the amplitude of the primary instabilities has considerably attenuated under $\lambda_d = 6$ and 8.5 mm disks. The growth of the primary instability is attenuated during the stage where the air gap is very small (hence the forcing effect is expected to be significant due to a higher pressure gradient) and coincidentally, it is also at the time when the overall water cavity starts to retract ($\tau < 1$ ms). As discussed previously, the forcing with short λ_d appears to be insufficient to overcome the surface tension and initiate the relatively short wavelengths. Therefore, the reduction in amplitude of the primary instability for short wavelength disks can be attributed to the attempt of the water surface to manifest a wavelength of λ_d which is unfavourable to be born and is connected to the overall retraction of the water cavity that elevates the water surface globally.

To compare the difference in growth rate for the wave-structured disks and a flat disk, the time derivative \dot{h} of Δh is taken from $\tau = 0.033$ ms to 0.5 ms [red solid line in panel (i)] and plotted in Fig. 4(b). For the short wavelength disks ($\lambda_d = 2$ –8.5 mm) that only give rise to primary instability, the growth rate declines rapidly with increasing λ_d , from 0.03 m/s for a flat disk to 0.006 m/s for $\lambda_d = 8.5$ mm. In contrast, for the disks that generate secondary instabilities ($\lambda_d = 12$ –34 mm), the growth rate increases gradually with the wavelength of the wave structures. In general, the growth rate of the primary instability for a wave-structured disk at the final stages before impact is always smaller than that of a flat disk of the same radius. It appears that imposing wave structures to modulate the wavelength of the forcing airflow on the water surface is damping the growth rate of the primary instabilities. Judging solely based on the amplitude of the primary instability shows no direct sign of resonance as the amplitude does not amplify when the imposed forcing wavelength coincides with the most unstable wavelength. We therefore now dive deeper and in addition turn to studying the characteristics of the secondary instabilities, that arise at a later stage around $\tau = 1.5$ ms and will be discussed next.

B. Wavelength of the instability

In search of indications of resonance, the wavelength of both the primary and the secondary instabilities on the water surface is quantified and compared. The instabilities are isolated from the cavity to better examine their wavelength. This is done by applying wavelet transform to break down the surface profile into several levels of a certain frequency range. With wavelet transform, the input signal, which is the surface profile is expressed as a linear combination of a set of scaled and translated copies of a wavelet function [21]. Wavelet transform has an advantage over Fourier transform in handling signals with finite lengths, which is the case for the surface profiles that are being studied here because the adaptive wavelet function has a finite length and can be scaled and translated. Due to the dominant wavelength being the wavelength of the water cavity, the Fourier spectrum gives a significantly high peak only for the wavelength corresponding to the entire water cavity. This is also why separation of the instabilities from the overall cavity shape is intended.

By taking the discrete wavelet transform (DWT) of the surface profile, the profile is compared with a chosen wavelet function to obtain the approximation and detail coefficients of the different levels. The surface profile is filtered into $N = 6$ levels, each with a wave number $1/\lambda$ range of $[\frac{1}{2^{N+1}\Delta_r}, \frac{1}{2^N\Delta_r}]$ where Δ_r is the spatial resolution and N is the index number of the level and a remainder $N + 1$ level that corresponds to the range of $[0, \frac{1}{2^{N+1}\Delta_r}]$ [21]. The choice of wavelet was based on the similarity of the wavelet function with the surface profile, and Symlets 5 is chosen. Parametric tests were done on the type of wavelet and the number of levels of decomposition, with comparable results. The original surface profile is well retrieved by adding back the decomposition. Besides, the empirical mode decomposition method was also tested and gave results that are similar to those obtained through wavelet transform; hence, the choice of decomposition method has minimal influence on the outcomes. Figure 5(a(i)) illustrates the decomposition of the original free-surface profile (black solid line) for a $\lambda_d = 17$ mm disk into three components:

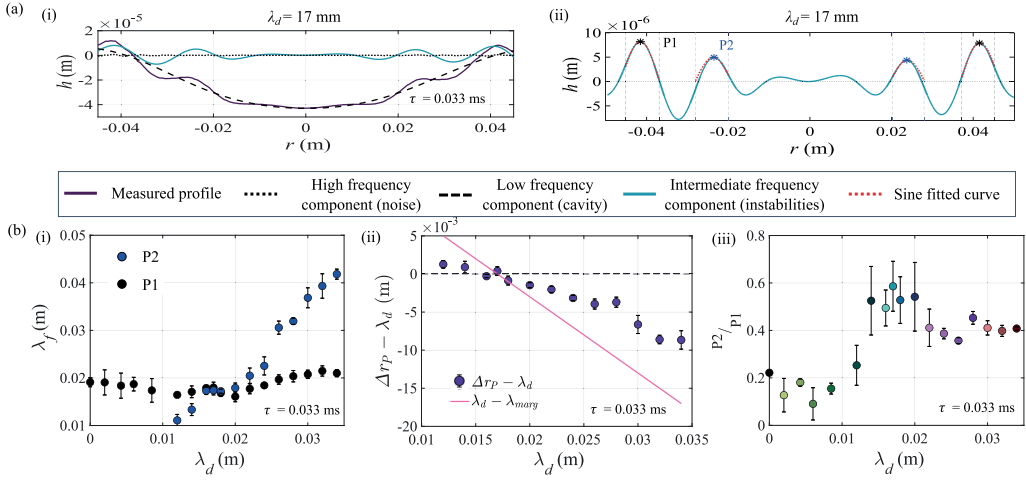


FIG. 5. (a) (i) Decomposition of the measured free-surface profile at $\tau = 0.033$ ms under a $\lambda_d = 17$ mm disk into high (noise, not shown), intermediate (instabilities) and low (overall cavity) frequencies by discrete wavelet transform. (ii) Estimation of the wavelength of instability, λ_f under the disk edge (P1) and under the subsequent crest on the disk (P2) by fitting the transformed profile to a sine-curve (red-dotted lines) locally. (b) (i) Estimated wavelength λ_f of P1 and P2 at $\tau = 0.033$ ms for all the disks. (ii) Difference between the distance Δr between the radial locations r_{P1} and r_{P2} of P1 and P2, respectively, on the one hand, and the wavelength of the disks λ_d , on the other hand. The pink solid line represents the difference $\lambda_d - \lambda_{\text{marg}}$ between the wavelength of each disk and the most unstable wavelength, $\lambda_{\text{marg}} = 17$ mm. (iii) Ratio of P2 to P1 as taken from the transformed profile of all the disks with different λ_d . Error bars show the standard deviation of the peak ratio over three repetitions of the experiment for each disk.

a high-frequency component which consists of short wavelengths smaller than 0.009 m (dotted line), a long wavelength component (>0.036 m) which corresponds to the cavity (dashed line) and the intermediate component (blue solid line) which contains the range of length in between, and corresponds to the wavelengths of interest. This will be called the transformed profile. Next, to estimate the wavelength of the instabilities (P1 and P2), the transformed profile is used and fitted to a sine-curve locally. This is done by taking the derivative of the transformed profile to locate the inflection points, which are the intersections between the transformed profile and the vertical dashed lines in Fig. 5(a(ii)), and subsequently that portion of the profile is fitted to a sine function to obtain the estimated wavelength of the instability λ_f for the primary instability P1 and the secondary instability P2.

A consistent length scale appears for the wavelength of the primary instability P1, which lies in the range of 0.0186 ± 0.002 m for all the disks as shown in Fig. 5(b(i)). The wavelength of the secondary instability, however, changes with the imprinted wavelength on the impacting disk. The wavelength of the secondary instabilities is similar to the imprinted wavelength, λ_d when they start to arise for the wave-structured disk with a wavelength λ_d of 12 and 14 mm. Meanwhile, it remains constant at approximately 0.017 m for wave-structured disks of $\lambda_d = 16$ –20 mm, which is the range of the disks with an imprinted wavelength close to the most unstable wavelength. The wavelength of the secondary instabilities then increases as the imprinted wavelength is further increased until 34 mm.

As mentioned previously in Sec. III, for disks with large imprinted wavelengths ($\lambda_d \geq 22$ mm), the secondary instabilities tend to moderately shift away from the crests, more towards the primary instabilities near the disk edge. To quantify this shifting behavior, the wavelength λ_d of each disk is subtracted from the distance between the radial location of the peaks of the primary r_{P1} and secondary r_{P2} instabilities, $\Delta r_P = r_{P1} - r_{P2}$, and plot the result against the wavelength λ_d imprinted

on the disk in Fig. 5(b(ii)) at $\tau = 0.033$ ms. If the distance between the two instabilities is the same as the imprinted wavelength on the disk, i.e., the instabilities are right under the crests, then the difference between Δr_P and λ_d will be zero which is indicated by the black horizontal dashed line. Meanwhile, the pink solid line represents the ideal condition where the distance between the two instabilities corresponds to the most unstable wavelength $\lambda_{\text{marg}} = 17$ mm irrespective of the imprinted wavelength on the disk. From here, it is evidenced that, the secondary instabilities for the longer wavelength disks ($\lambda_d \geq 22$ mm) shift from the crests as they deviate from the horizontal dashed line and incline towards the pink solid line, suggesting their tendency to manifest instabilities with an interval that is closer to 17 mm. It is also clear that the instabilities under the disks with intermediate wavelength ($12 \text{ mm} \leq \lambda_d \leq 20 \text{ mm}$) closely align with the crests as they are close to the horizontal dashed line. One point to highlight here is the similarity of the distance between the two instabilities with each other and also with the most unstable wavelength when the imprinted wavelength on the disk is around 17 mm.

To see how the amplitude of the secondary instability compares to that of the primary instability, the amplitude ratio of the secondary and primary instability P2/P1 is obtained from the transformed profiles for all the disks and are plotted in Fig. 5(b(iii)). For the short wavelength disks, as the secondary instabilities are not aroused, the amplitude ratio remains low. The amplitude ratio P2/P1 increases above 0.5 when the wavelength λ_d imprinted on the impacting disk is around the most unstable wavelength $\lambda_{\text{marg}} = 0.017$ m, suggesting a resonant response of the system when the wavelength of the modulated base airflow matches with the most unstable wavelength. Note that, when the amplitude ratio peaks around this most unstable wavelength ($\lambda_d = 0.016\text{--}0.020$ m), the fitted wavelengths λ_f of both P1 and P2 are almost identical as shown in Fig. 5(b(i)). This further supports the hypothesis that the secondary instabilities are excited due to resonance. Subsequently, the amplitude ratio decreases slightly and remains relatively constant at around 0.4 for the disks with wave structures of longer wavelength.

These results on the length scale and the amplitude ratio of the instabilities have several important implications. First, it shows that the nature of the instabilities complies with an instability of the Kelvin-Helmholtz type. With the modulation of the airflow, the short wavelength waves do not arise on the water surface under forcing due to the stabilizing effect of surface tension, and the long wavelength waves, although developed under the imposed forcing, are small in amplitude as compared to the primary instabilities with the wavelength similar to the most unstable wavelength. Therefore, the instability induced under a horizontal flat disk prior to impact can be regarded as Kelvin-Helmholtz instability, initiated by the rapid airflow that exceeds a critical velocity with only the unstable wavelengths being manifested. Second, it suggests that the subsequent growth and development of the instability on the interface can be modulated through a resonance mechanism. When the wavelength imprinted on the impacting disk λ_d is close to the most unstable wavelength λ_{marg} , a pressure distribution that is of the same frequency with the most unstable wavelength is formed at the interface, supplying the energy to sustain the growth and development of the instability.

V. IMPACT OF THE WAVE-STRUCTURED DISK INTO WATER

A. Impact process

A second question we want to address in this work is to what extent the entrapment of air below the wave-structured disks influences the impact load that is experienced by them. To do so, we record the impact process of the wave-structured disks into the water bath from the bottom. Disks with a wavelength of $\lambda_d = 2, 17, \text{ and } 34$ mm are chosen as representative disks with a short, intermediate and long wavelength respectively and five snapshots of the impact process are depicted in Fig. 6. Disks with different lengths of imprinted wavelengths exhibit a different propagation behavior of the waterfront. Here, it is good to note that the total volume of air present between the crests of the wave structure V_{hole} is approximately equal to $\pi a_0 R^2$; it deviates less than 5% from this value. However,

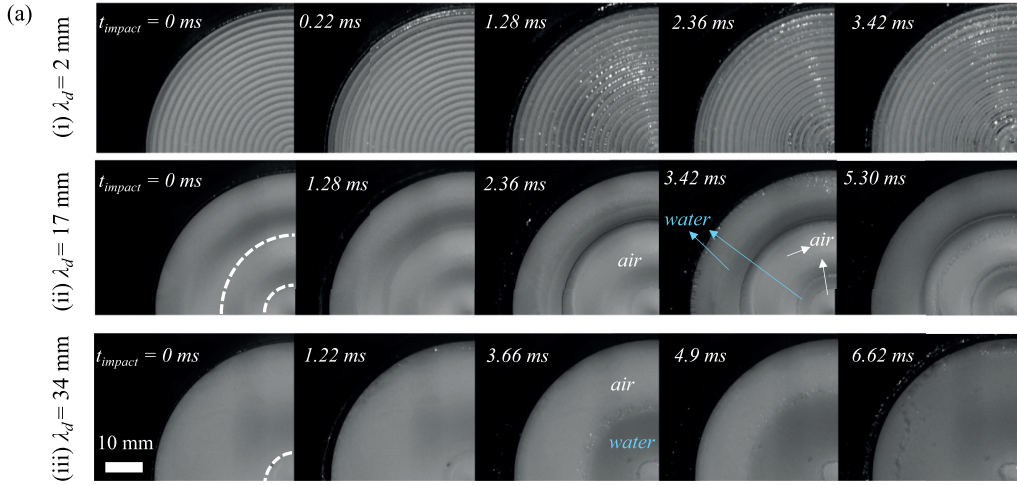


FIG. 6. (a) Snapshots of the impact process of a disk with (i) $\lambda_d = 2$ mm, (ii) $\lambda_d = 17$ mm and (iii) $\lambda_d = 34$ mm, recorded at 50 000 f.p.s. from the bottom. $t_{\text{impact}} = 0$ ms is the time at which the edge of the disks made contact with the water surface. With the disk edge being the first crest for all the disks, the dashed lines in the first images of (ii) and (iii) indicate the subsequent crests of the wave structure on the disk. A quarter of the disks are shown to get a better sight of the solid-liquid contact region and the water-air interface on the disk during impact. The surface of the disk that is wetted with water appears to be darker in the images while the brighter regions indicate a solid-air contact. Refer to Ref. [20] for false colored images to better visualize the wetted and nonwetted areas. Videos of the impact process featuring the whole disk as viewed from the bottom are also included in the Supplemental Material [20].

depending on the wavelength λ_d , the distribution of the air volume could be very different. From Fig. 6(i), for a $\lambda_d = 2$ mm disk, it is observed that when the water makes initial contact with the disk edge at $t_{\text{impact}} = 0$ ms, the waterfront from the disk edges starts to propagate inwards to the center of the disk and wets almost all of the disk surface at $t_{\text{impact}} = 1.28$ ms. The solid-air and solid-water contact regions can be differentiated by the brighter regions at the solid-air contact and darker shades for the solid-water contact in the images. The size of the entrapped air pocket within the troughs of the wave structures is small due to the small wavelength of the wave structures. As the waterfront propagates inwards with time, the water penetrates into the small wave troughs relatively easily and the small air pockets can be seen to be expelled from the troughs at $t_{\text{impact}} \geq 1.28$ ms. Meanwhile for an intermediate wavelength disk ($\lambda_d = 17$ mm, Fig. 6(ii)), while the waterfront slowly propagates from the disk edges towards the disk center after $t_{\text{impact}} = 0$ ms, the second and third wave crest starts to make contact with the water surface at $t_{\text{impact}} = 1.28$ ms and 2.36 ms respectively. At this point, most of the disk surface is still cushioned by the entrapped air. The waterfronts from the second and third wave crests expand mainly outward towards the disk edges. Subsequently, the trapped air between the disk edge and the second crest is pushed towards the disk edge when the moving waterfront started from the second wave crest reaches the adjacent wave trough. The size of the air pocket under the disk at $t_{\text{impact}} = 5.30$ ms, mainly entrapped between the second and third wave crests, is larger as compared to a small wavelength disk. A similar propagation pattern is also observed for a long wavelength disk as shown in Fig. 6(iii) where the waterfront expands outward after the second wave crest touches the water surface at $t_{\text{impact}} = 1.22$ ms. The wetted area of the disk is seen to increase quickly due to the outward propagation of the waterfront from the second wave crests that pushes the air towards the edges. This results in a large solid-water contact; hence, less air is retained under the disk at the end of the impact process.

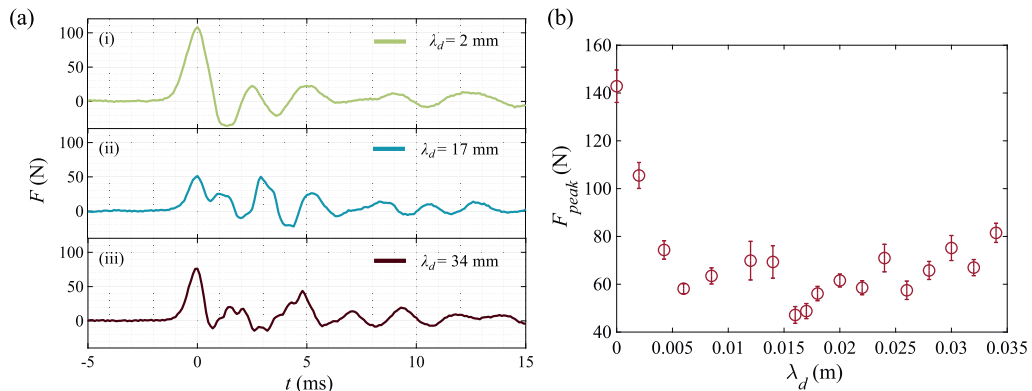


FIG. 7. (a) Time evolution of the force experienced by the disk during impact, measured for (i) $\lambda_d = 2$ mm, (ii) $\lambda_d = 17$ mm, and (iii) $\lambda_d = 34$ mm disks at $U_0 = 1.0$ m/s. The signals are centered around $t = 0$ ms when the impact force reaches its first peak for each disk. (b) First peak impact force measured for all the disks with different λ_d . Error bars show the standard deviation of the first peak impact force over 10 repetitions of the experiment.

B. Impact force measurement

The impact force over the whole surface of the impacting disk is measured over time, and the results for three selected disks ($\lambda_d = 2, 17,$ and 34 mm) are plotted in Fig. 7(a). The impact force measurement taken by the load cell is the averaged force throughout the disk and rod assembly due to the configuration of the experimental setup. Here, the force signals are centered about $t = 0$ ms when the impact force reaches its first peak for each disk. Thus, the impact time t_{impact} , defined as the time at which the disk edge first comes in contact with the water surface in the previous sections (and in those sections identified with $\tau = 0$) now corresponds to some negative time where the force signal starts to rise above 0 N in current plots. Here, one should realize that the force already starts rising before the first contact, where the force is mediated by the intervening air layer [9].

The characteristic of the initial added-mass induced force peak for a wave-structured disk is different from a flat disk and varies for the disks with different imprinted wavelengths. This is due to the difference in the profile of the contact surface which gives discrete expansion rates of the wetted area. Previous studies showed that increasing the deadrise angle of a wedge increases the duration of the impact peak [22] and the time scale of the impact peak also alters with the curvature of the impacting disk, with convex and concave surfaces dilating the duration of the force peak [8]. During disk impact, entrapped air provides a cushioning effect which delays the time for the impact force to reach its first maximum ($t = 0$ ms) after the initial contact with the water surface [9]. Due to the surface curvature, the duration of the force peak for a wave-structured disk is always longer than that for a flat disk, simply because in principle one needs a time $\sim \frac{\lambda_d}{U_0}$ for the disk to come into full contact with the disk, even in the absence of air. For a short wavelength disk, e.g., $\lambda_d = 2$ mm, the impact force gives a single primary peak that reaches its maximum at about 2 ms after the initial contact with water, which is when the disk surface is largely wetted by water as observed from the bottom view. Meanwhile, for the $\lambda_d = 17$ and 34 mm disks, several impact force peaks were observed which extended the impact duration. The force signal for a large wavelength disk ($\lambda_d = 34$ mm) features a primary peak that is considerably larger in magnitude than the subsequent peaks. The impact force peaks at approximately 1 ms after the first contact, which agrees with the time interval at which the subsequent crest after the disk edge also comes into contact with the water surface. Meanwhile, for an intermediate wavelength disk, e.g., $\lambda_d = 17$ mm, two force peaks are seen in the first 3 ms after the initial contact, which also corresponds to the time at which the subsequent two

crests touch the water surface. A secondary force peak, which is of the second highest magnitude in the measured signal also appears at $t = 3$ ms and 5 ms respectively for the disks with a wavelength of 17 and 34 mm. The time is very close to the instant where the waterfront expanding from the second crests pushes the entrapped air out to the disk edge as seen from the bottom view, increasing the wetted area of the disk. In general, the force signals give a fairly good qualitative agreement with the previous observation from the bottom throughout the impact process. It must be emphasized that the subsequent force signal after $t = 0$ ms is also affected by the structural oscillation of the disk and rod system and on a longer time scale, by sloshing in the water reservoir after the impact.

Next, the magnitude of the peak impact force for all the disks is compared in Fig. 7(b). It is prominent that having a wave structure on the impacting disk significantly reduces the peak impact force, which is around 140 N for a flat disk of the same radius $R = 40$ mm by approximately a factor of 2, provided the air is entrapped and retained effectively under the disk during the impact process. The degree of reduction in impact force is relatively mild for a $\lambda_d = 2$ mm disk ($F_{\text{peak}} = 105.5$ N) due to the fact that the air pocket ruptures during the impact and the wetted area is still very much comparable to the case of a horizontal flat disk as observed from the experiment. The magnitude of the peak impact force for the other wave-structured disk is almost half of the peak impact force on a flat disk, fluctuating between 47.1 and 81.5 N.

The influence of the total volume of voids on the wave-structured disks on the maximum impact force is first examined. The experimental results are compared with the model proposed in Ref. [16] that predicts the impact force's time evolution and the maximum impact force of a surface-patterned disk impacting onto an undeformed liquid surface based on the total volume of trapped air in the voids of the disk. The theoretical model proposed in Ref. [16] predicts a maximum impact force of approximately 150 N for all the wave-structured disks. This prediction is consistently overestimating the actual impact force observed in our experiment (see the Supplemental Material [20]). Nevertheless, from a qualitative standpoint, what could be concluded from the model in Ref. [16] is that the maximum impact force of a wave-structured disk is expected to be lower than a flat disk due to air-cushioning and to be rather consistent for all the wave-structured disks since they have a similar total void volume. This does not completely agree with our experimental results, where the $\lambda_d = 2$ mm disk has a relatively higher maximum impact force than the other wave-structured disks, even though the volume of voids is the same for the $\lambda_d = 2$ and 20 mm disks. Therefore, it is clear that the difference in the total void volume on the disk is not the main factor for the discrepancy in the maximum impact force for the wave-structured disks. In Ref. [16], the maximum impact force on meshlike surface patterned disks is found to be characterized by the total volume of entrapped air under the disks, independent of the regular or irregular shape/arrangement of the meshlike pattern on their impacting disk. This is due to the reason that despite the irregularity of the meshlike pattern, all the surface-patterned disks have a vertically straight wall; hence, the simplification of the averaged water penetration velocity into the disk voids to one dimension in the model is reasonable. However, for our wave-structured disks, this does not apply because of the varying slopes of the wave structure with the wavelengths; hence, such model could not capture the influence of the inertial wetting velocity along the wave structure. In addition, the fact that the model predicted a higher value than the experimentally observed force suggests that the pressure build-up in the air voids is less than what was theoretically predicted, which in turn could be explained by air being expelled from the voids during the impact process, in line with what we have observed in the bottom-view recordings of the impact.

The expulsion of air from the voids will depend on the penetration of water into the voids of the wave-structured disk. Hence, to compare the inertial wetting velocity on the wave structure of different wavelengths, the flow on the wave-structure surface during impact is approximated as a half-body potential flow, which is the superposition of a uniform flow toward the structure at the impact velocity U_0 and a source with a source strength $m = 2\pi bU_0$, where b is the location of the source from stagnation point. The location of the source from the stagnation point is dependent on the wavelength of the disk by $b = \lambda_d/2\pi$. With the coordinates defined in Fig. 8(a), the origin always coincides with the location of the source. Then, the velocity on the surface V_{surf} (relative to

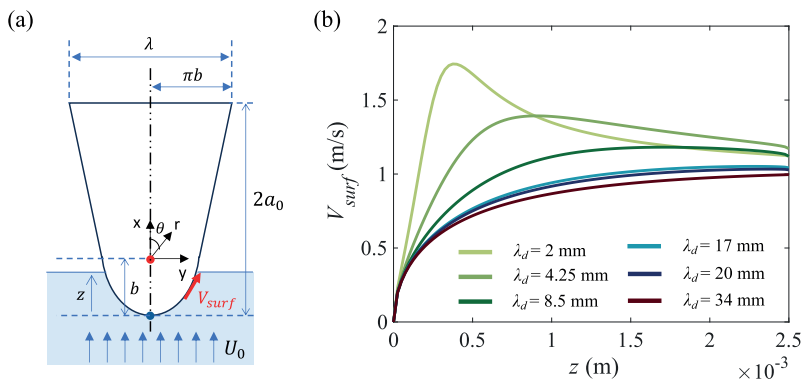


FIG. 8. (a) Schematic of the half-body potential flow to estimate the inertial wetting velocity on a single wave structure V_{surf} . (b) Velocity on the surface of the wave structure V_{surf} of several selected wavelengths at different heights of penetration into the voids z .

the disk) can be obtained by

$$V_{surf}^2 = U_0^2 \left(1 + \frac{2b \cos \theta}{r} + \frac{b^2}{r^2} \right), \quad (7)$$

which is a typical textbook problem. The surface profile of the wave-structure disk is described as

$$S(y) = a_0 - a_0 \cos \left(\frac{2\pi y}{\lambda_d} \right). \quad (8)$$

Here, we let the height of penetration into the voids be $z(t)$. Hence, the wetted height along the surface x following the coordinate system defined in Fig. 8(a) will be $x(t) = z - b$ and the wetted width y can be found by equating $S(y) = z$. Since $y = r \sin \theta$ and $x = r \cos \theta$, the velocity along the surface V_{surf} can then be obtained from Eq. (7) by substituting the value of r and θ . As shown in Fig. 8(b), the velocity on a wave structure with short wavelength ($\lambda_d = 2$ and 4.25 mm) increases rapidly as z increases and reaches a maximum, shortly after passing the location of the source. Meanwhile, the increase in velocity along the intermediate and long wavelength wave-structure surfaces are similar, with a less steep gradient and tend to reach a plateau. Therefore, the liquid is expected to penetrate quicker into the voids on the disk with a shorter imprinted wavelength at the initial stage and compress the entrapped air. As the pressure builds up within the voids, the compressed air will escape from the voids on the disk. The compressed air that is exerted on the water surface, together with the wetted region of the disk, displaces the added mass of the liquid which accounts for the initial impact force experienced by the disk. Since the process occurs faster for a disk with a short wavelength, the resulting impact force is expected to be higher at the initial stage. Meanwhile, for the disks with an intermediate or long imprinted wavelength, the liquid flows into the voids at a more gradual pace which could potentially slow down the compression and decompression of the entrapped air pocket and prolong the retention of the air within the voids, resulting in a lower initial peak force.

The experimental results and the analysis above suggest that the interplay of surface-wetting behavior in combination with the retention of the initially trapped air during the impact is crucial in determining the impact force exerted on a disk. In addition, the effect of the free-surface deformation prior to impact should not be overlooked as the experimental results show a small peak impact force when the imprinted wavelength on the disk is close to the most unstable wavelength λ_{marg} . The impact of a wave-structured disk is complicated by the fact that each wave-structured disk has a different number of wave structures depending on the imprinted wavelength. Therefore, even though the total volume of voids on the disks is similar, they have very different void volume distributions

under the disk. Besides, the change in the slope of the wave structure on the disk resulting from the variation in the imprinted wavelength will also have an influence on the evolution of the free surface along the wave structure's surface. The free-surface evolution is critical in determining both the wetted and unwetted areas on the disk, which exerts a significant influence on the resultant impact force [23]. In addition, the mismatch between the imposed wavelength λ_d and the disk radius leads to poorly comparable boundary conditions near the center of the disk for varying λ_d . On top of that, the measured impact force is the average over the whole disk surface that could not provide very well-resolved information on the influence of wave structure on the impact force. Despite these complications, the experimental results confirm the effect of air-cushioning in reducing the peak impact force by distributing the hydrodynamics load over an extended duration. It also shows that the inertial wetting velocity along the wave structure and thus, the evolution of the wetted area could influence the peak impact force. Moreover, when the total entrapped volume of air within the disk voids is the same, the peak impact force on a wave-structured disk is found to be consistently lower than a meshlike structured disk studied in Ref. [16]. The reduction is particularly pronounced for the wave-structured disks with an intermediate and longer wavelength, where the magnitude is around or less than half of the predicted peak impact force for a meshlike structured disk in Ref. [16]. Therefore, a shallow, smooth wave structure on the impacting disk is anticipated to be more effective in mitigating the peak impact force.

VI. CONCLUSION

In conclusion, the growth of the free-surface instability prior to the impact of a wave-structured disk and the characteristic of the impact force loading on the disk during the impact process are investigated. By imposing a radially symmetric wave structure of different wavelengths on the impacting disk, the escaping airflow between the disk and the free water surface is modulated to create an airflow with local velocity maxima and minima that exerts a forcing on the water surface. The free surface prior to impact is measured experimentally with a TIR-based measurement technique and results show that a short wavelength wave structure on the impacting surface of the disk attenuates the amplitude of the primary instability under the disk edge. Secondary instabilities appear within the preimpact water cavity for the disks with intermediate and long wavelength wave structures. The amplitude of the secondary instabilities is amplified when the imprinted wavelength on the disk is close to the theoretical dominant unstable wavelength $\lambda_{\text{marg}} \approx 0.017$ m derived from the linearized Kelvin-Helmholtz stability analysis. This can be attributed to a resonance effect, where the air pressure distribution under the disk is in phase with the dominant unstable wavelength and sustains the growth of the instability when the wavelength on disk λ_d is close to the most unstable wavelength λ_{marg} . In addition, the fact that the wavelength of both primary and secondary instabilities are almost identical when the amplitude ratio of P2/P1 has a maximum further substantiates the hypothesis that the secondary instabilities developed due to resonance. The nature of the free-surface instability under an impacting disk complies with an instability of the Kelvin-Helmholtz type as the wavelength of the primary instability is 0.0186 ± 0.002 m, consistently around the dominant unstable wavelength. It is further supported by the fact that capillary waves of short wavelength did not arise under forcing with small wavelength structures on the disk. Although secondary instabilities of a long wavelength arise under the disks with a longer wavelength, their amplitude is small when compared to the primary instability and they tend to shift toward a distance closer to 0.017 m from the primary instability. Further research could investigate the influence of surface tension by substituting the liquid used by one with a smaller surface tension. Besides, while current experiments focused on the inertial regime, further experiments could use a broader range of impact velocities to explore the transition to the viscous flow regime and its influence on surface instability.

The role of air in mitigating the peak impact force is prominent as the peak impact force on a wave-structured disk with voids to entrap more air is halved as compared to a flat disk of the same radius. However, the duration of the impact force peak is lengthened for a wave-structured disk.

Based on the experimental results, the wetting behavior on the impacting surface that changes with the imprinted wavelength on the disk and the amount of air that is well entrapped throughout the impact process is crucial in determining the evolution of the impact force exerted on a disk. As compared to a meshlike structured disk, a shallow and smooth wave structure promotes a relatively gradual inertial wetting of the impacting surface during the impact process, leading to a lower peak impact force.

ACKNOWLEDGMENTS

This publication is part of the Vici project IMBOL (Project No. 17070) and SLING (Project No. P14-10.1) which are partly financed by the Dutch Research Council (NWO). We thank A. Prosperetti for helpful discussions. We also thank G.-W. Bruggert and M. Bos for their technical support.

-
- [1] T. Von Karman, *The Impact on Seaplane Floats During Landing*, Tech. Note 321 (National Advisory Committee on Aeronautics, Washington, DC, 1929).
 - [2] S. Abrate, Hull slamming, *Appl. Mech. Rev.* **64**, 060803 (2011).
 - [3] D. Peregrine, Water-wave impact on walls, *Annu. Rev. Fluid Mech.* **35**, 23 (2003).
 - [4] F. Dias and J.-M. Ghidaglia, Slamming: Recent progress in the evaluation of impact pressures, *Annu. Rev. Fluid Mech.* **50**, 243 (2018).
 - [5] J.-S. Koh, E. Yang, G.-P. Jung, S.-P. Jung, J. H. Son, S.-I. Lee, P. G. Jablonski, R. J. Wood, H.-Y. Kim, and K.-J. Cho, Jumping on water: Surface tension–dominated jumping of water striders and robotic insects, *Science* **349**, 517 (2015).
 - [6] J. Verhagen, The impact of a flat plate on a water surface, *J. Ship Res.* **11**, 211 (1967).
 - [7] H. C. Mayer and R. Krechetnikov, Flat plate impact on water, *J. Fluid Mech.* **850**, 1066 (2018).
 - [8] E. Ermanyuk and N. Gavrilov, Experimental study of disk impact onto shallow water, *J. Appl. Mech. Tech. Phys.* **52**, 889 (2011).
 - [9] U. Jain, P. Vega-Martínez, and D. Van Der Meer, Air entrapment and its effect on pressure impulses in the slamming of a flat disc on water, *J. Fluid Mech.* **928**, A31 (2021).
 - [10] L. S. Cohen and T. J. Hanratty, Generation of waves in the concurrent flow of air and a liquid, *AIChE J.* **11**, 138 (1965).
 - [11] O. M. Phillips, On the generation of waves by turbulent wind, *J. Fluid Mech.* **2**, 417 (1957).
 - [12] U. Jain, A. Gauthier, D. Lohse, and D. van der Meer, Air-cushioning effect and Kelvin-Helmholtz instability before the slamming of a disk on water, *Phys. Rev. Fluids* **6**, L042001 (2021).
 - [13] D. van der Meer, Linear stability analysis of a time-divergent slamming flow, *J. Fluid Mech.* **934**, A4 (2022).
 - [14] M. Hattori, A. Arami, and T. Yui, Wave impact pressure on vertical walls under breaking waves of various types, *Coastal Eng.* **22**, 79 (1994).
 - [15] S.-L. Chuang, Experiments on flat-bottom slamming, *J. Ship Res.* **10**, 10 (1966).
 - [16] T. Kim, D. Kim, and D. Kim, Water impact of a surface-patterned disk, *J. Fluid Mech.* **915**, A52 (2021).
 - [17] S. Okada and Y. Sumi, On the water impact and elastic response of a flat plate at small impact angles, *J. Mar. Sci. Technol.* **5**, 31 (2000).
 - [18] E. Ermanyuk and M. Ohkusu, Impact of a disk on shallow water, *J. Fluids Struct.* **20**, 345 (2005).
 - [19] U. Jain, A. Gauthier, and D. van der Meer, Total-internal-reflection deflectometry for measuring small deflections of a fluid surface, *Exp Fluids* **62**, 235 (2021).
 - [20] See Supplemental Material at <http://link.aps.org/supplemental/10.1103/PhysRevFluids.9.010501> for the deformation at the free surface for all the other disks (Sec. I), the plot of pressure distribution derived by integrating Eq. (6) (Sec. II), the colored images of the impacting disks in Fig. 6 to illustrate the wetted

- area (Sec. III), the comparison with the theoretical force model in Ref. [16] (Sec. IV) and the video of the impact process viewed from the bottom (Video 1).
- [21] D. B. Percival and A. T. Walden, *Wavelet Methods for Time Series Analysis*, Vol. 4 (Cambridge University Press, Cambridge, UK, 2000).
- [22] L. Vincent, T. Xiao, D. Yohann, S. Jung, and E. Kanso, Dynamics of water entry, *J. Fluid Mech.* **846**, 508 (2018).
- [23] T. Khabakhpasheva, A. Korobkin, and S. Malenica, Fluid impact onto a corrugated panel with trapped gas cavity, *Appl. Ocean Res.* **39**, 97 (2013).